7. Whittaker, M. *et al.* A 35 Å movement of smooth muscle myosin on ADP release. *Nature* **378,** 748–751 (1995).
8. Mooseker, M. S. & Cheney, R. E. Unconventional myosins. *Annu. Rev. Cell Dev. Biol.* **11,** 633–675 (1995).
9. Kellerman, K. A. & Miller, K. G. An unconventional myosin heavy chain gene from *Drosophila melanogaster*. *J. Cell Biol.* **119,** 823–834 (1992).
10. Hasson, T. & Mooseker, M. S. Porcine myosin VI: characterization of a new mammalian unconventional myosin. *J. Cell Biol.* **127,** 425–440 (1994).
11. Avraham, K. B. *et al.* The mouse Snell's waltzer deafness gene encodes an unconventional myosin required for structural integrity of inner ear hair cells. *Nature Genet.* **11,** 369–375 (1995).
12. Avraham, K. B. *et al.* Characterization of human unconventional myosin-VI, a gene responsible for deafness in Snell's waltzer mice. *Hum. Mol. Genet.* **6,** 1225–1231 (1997).
13. Hasson, T. *et al.* Unconventional myosins in inner-ear sensory epithelia. *J. Cell Biol.* **137,** 1287–1307 (1997).
14. Buss, F. *et al.* The localization of myosin VI at the Golgi complex and leading edge of fibroblasts and its phosphorylation and recruitment into membrane ruffles of A431 cells after growth factor stimulation. *J. Cell Biol.* **143,** 1535–1545 (1998).
15. Mermall, V., McNally, J. G. & Miller, K. G. Transport of cytoplasmic particles catalysed by an unconventional myosin in living *Drosophila* embryos. *Nature* **369,** 560–562 (1994).
16. Kron, S. J. & Spudich, J. A. Fluorescent actin filaments move on myosin fixed to a glass surface. *Proc. Natl Acad. Sci. USA* **83,** 6272–6276 (1986).
17. Wolenski, J. S., Cheney, R. E., Mooseker, M. S. & Forscher, P. *In vitro* motility of immunoadsorbed brain myosin-V using a *Limulus* acrosomal process and optical tweezer-based assay. *J. Cell Sci.* **108,** 1489–1496 (1995).
18. Jontes, J. D., Wilson-Kubalek, E. M. & Milligan, R. A. A 32 degree tail swing in brush border myosin I on ADP release. *Nature* **378,** 751–753 (1995).
19. Henningsen, U. & Schliwa, M. Reversal in the direction of movement of a molecular motor. *Nature* **389,** 93–96 (1997).
20. Sablin, E. P. *et al.* Direction determination in the minus-end-directed kinesin motor ncd. *Nature* **395,** 813–816 (1998).
21. Endow, S. A. & Waligora, K. W. Determinants of kinesin motor polarity. *Science* **281,** 1200–1202 (1998).
22. Hirose, K., Cross, R. A. & Amos, L. A. Nucleotide-dependent structural changes in dimeric NCD molecules complexed to microtubules. *J. Mol. Biol.* **278,** 389–400 (1998).
23. Sosa, H. *et al.* A model for the microtubule-Ncd motor protein complex obtained by cryo-electron microscopy and image analysis. *Cell* **90,** 217–224 (1997).
24. Sweeney, H. L. *et al.* Kinetic tuning of myosin via a flexible loop adjacent to the nucleotide binding pocket. *J. Biol. Chem.* **273,** 6262–6270 (1998).
25. Hopp, T. P. *et al.* A short polypeptide marker sequence useful for recombinant protein identification and purification. *Biotechnology* **6,** 1205–1210 (1988).
26. Kolodziej, P. A. & Young, R. A. Epitope tagging and protein surveillance. *Methods Enzymol.* **194,** 508–519 (1991).
27. Espreafico, E. M. *et al.* Primary structure and cellular localization of chicken brain myosin-V (p190), an unconventional myosin with calmodulin light chains. *J. Cell Biol.* **119,** 1541–1557 (1992).
28. Pollard, T. D. Assays for myosin. *Methods Enzymol.* **85,** 123–130 (1982).
29. Elzinga, M. & Phelan, J. J. F-actin is intermolecularly crosslinked by N,N′-*p*-phenylenedimaleimide through lysine-191 and cysteine-374. *Proc. Natl Acad. Sci. USA* **81,** 6599–6602 (1984).
30. Jontes, J. D. & Milligan, R. A. Brush border myosin-I structure and ADP-dependent conformational changes revealed by cryoelectron microscopy and image analysis. *J. Cell Biol.* **139,** 683–693 (1997).

Acknowledgements

This work was supported by grants from the NIH. We thank M. S. Mooseker for the chicken myosin V cDNA, and G. Daniels of Leica Microsystems for technical support.

Correspondence and requests for materials should be addressed to H.L.S. (e-mail: Lsweeney@mail.med.upenn.edu).

erratum

Changing spatial structure of the thermohaline circulation in response to atmospheric CO_2 forcing in a climate model

Richard A. Wood, Ann B. Keen, John F. B. Mitchell & Jonathan M. Gregory

Nature **399,** 572–575 (1999)

The scale vectors shown at the bottom left of each panel in Fig. 2 were the wrong size as published; the corrected figure is shown below.

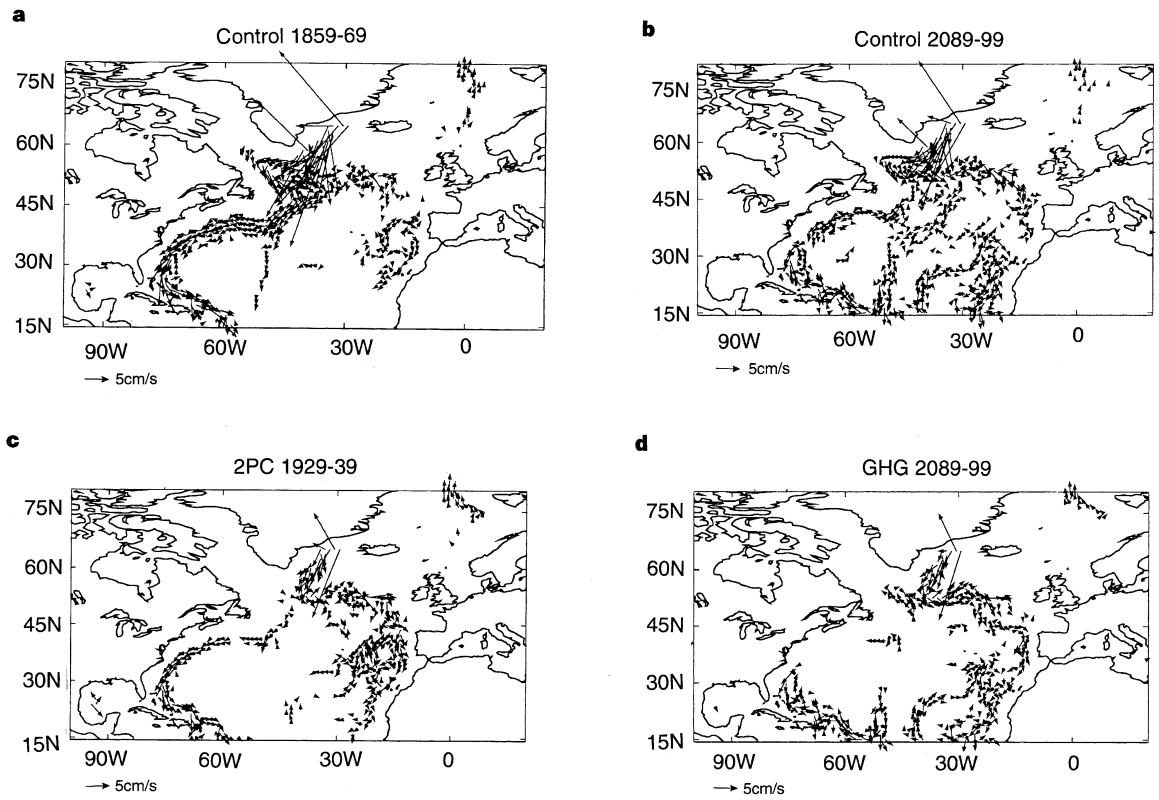

uncertainty analysis included any uncertainty due to the finite length of data used to derive the optimisation. For consistency with earlier work[21–24], we have used standard estimates of pattern amplitudes based on linear regression which are biased towards zero[25] when, as here, there is uncertainty in the signals.

Bearing in mind these caveats, we interpret our results as showing the following: first, the temperature changes over the twentieth century cannot be explained by any combination of natural internal variability and the response to natural forcings alone. Second, the recent warming, ~0.25 K, can be explained by the response of the climate to anthropogenic changes in greenhouse-gas concentrations partly offset by cooling due to anthropogenic sulphate aerosols, resulting in little net temperature change from 1946 to the mid-1970s. Last, the warming early this century can also be explained by anthropogenic causes and internal variability. However, solar irradiance changes could have made a significant contribution, ~0.125 K, if we assume little error in the relative amplitude of the forcing of sulphates and greenhouse gases prescribed in our model. □

Received 5 October 1998; accepted 25 March 1999.

1. Parker, D. E., Jones, P. D., Folland, C. K. & Bevan, A. Interdecadal changes of surface temperature since the late nineteenth century. *J. Geophys. Res.* **99,** 14373–14399 (1994).
2. Stouffer, R. J., Manabe, S. & Vinnikov, K. Y. Model assessment of the role of natural variability in recent global warming. *Nature* **367,** 634–636 (1994).
3. Santer, B. D. *et al.* A search for human influences on the thermal structure of the atmosphere. *Nature* **382,** 39–45 (1996).
4. Tett, S. F. B., Mitchell, J. F. B., Parker, D. E. & Allen, M. R. Human influence on the atmospheric vertical temperature structure: Detection and observations. *Science* **247,** 1170–1173 (1996).
5. Hegerl, G. C. *et al.* Multi-fingerprint detection and attribution analysis of greenhouse gas, greenhouse gas-plus-aerosol and solar forced climate change. *Clim. Dyn.* **13,** 613–634 (1997).
6. Johns, T. C. *et al.* The second Hadley Centre coupled ocean-atmosphere GCM: Model description, spinup and validation. *Clim. Dyn.* **13,** 103–134 (1997).
7. Tett, S. F. B., Johns, T. C. & Mitchell, J. F. B. Global and regional variability in a coupled AOGCM. *Clim. Dyn.* **13,** 303–323 (1997).
8. Shine, K. P., Fouquart, Y., Ramaswamy, V., Solomon, S. & Srinivasan, J. in *Climate Change 1995: the Science of Climate Change* (eds Houghton, J. T. *et al.*) 108–118 (Cambridge Univ. Press, 1996).
9. Mitchell, J. F. B., Johns, T. C., Gregory, J. M. & Tett, S. F. B. Climate response to increasing levels of greenhouse gases and sulphate aerosols. *Nature* **376,** 501–504 (1995).
10. Mitchell, J. F. B. & Johns, T. C. On modification of global warming by sulfate aerosols. *J. Clim.* **10,** 245–267 (1997).
11. Mitchell, J. F. B., Davis, R. A., Ingram, W. J. & Senior, C. A. On surface temperature, greenhouse gases, and aerosols: Models and observations. *J. Clim.* **10,** 2364–2386 (1995).
12. Langner, J. & Rodhe, H. A global three-dimensional model of the tropospheric sulfur cycle. *J. Atmos. Chem.* **13,** 225–263 (1991).
13. Twomey, S. A. Pollution and the planetary albedo. *Atmos. Environ.* **8,** 1251–1256 (1974).
14. Albrecht, B. A. Aerosols, cloud microphysics and fractional cloudiness. *Science* **245,** 1227–1230 (1989).
15. Sato, M., Hansen, J. E., McCormick, M. P. & Pollack, J. B. Stratospheric aerosol optical depths (1850–1990). *J. Geophys. Res.* **98,** 22987–22994 (1993).
16. Hoyt, D. V. & Schatten, K. H. A discussion of plausible solar irradiance variations, 1700–1992. *J. Geophys. Res.* **98,** 18895–18906 (1993).
17. Willson, R. C. Total solar irradiance trend during solar cycles 21 and 22. *Science* **277,** 1963–1965 (1997).
18. Stott, P. A. & Tett, S. F. B. Scale-dependent detection of climate change. *J. Clim.* **11,** 3282–3294 (1998).
19. Haywood, J., Stouffer, R., Wetherald, R., Manabe, S. & Ramaswamy, V. Transient response of a coupled model to estimated changes in greenhouse gas and sulfate concentrations. *Geophys. Res. Lett.* **24,** 1335–1338 (1997).
20. Ramaswamy, V. & Chen, C.-T. Linear additivity of climate response for combined albedo and greenhouse perturbations. *Geophys. Res. Lett.* **24,** 567–570 (1997).
21. Hasselmann, K. Optimal fingerprints for the detection of time-dependent climate change. *J. Clim.* **6,** 1957–1971 (1993).
22. Hasselmann, K. Multi-pattern fingerprint method for detection and attribution of climate change. *Clim. Dyn.* **13,** 601–611 (1997).
23. North, G. R., Kim, K.-K., Shen, S. S. P. & Hardin, J. W. Detection of forced climate signals. Part I: filter theory. *J. Clim.* **8,** 401–408 (1995).
24. Allen, M. R. & Tett, S. F. B. Checking for model consistency in optimal fingerprinting. *Clim. Dyn.* (in the press).
25. Mardia, K. V., Kent, J. T. & Bibby, J. M. *Multivariate Analysis* (Academic, London, 1979).
26. Lean, J., Beer, J. & Bradley, R. Reconstruction of solar irradiance since 1610: implications for climate change. *Geophys. Res. Lett.* **22,** 3195–3198 (1995).
27. Haigh, J. D. Impact of solar variability on climate. *Science* **272,** 981–984 (1996).
28. Haigh, J. D. The role of stratospheric ozone in modulating the solar radiative forcing of climate. *Nature* **370,** 544–546 (1994).

Supplementary information is available on *Nature*'s World-Wide Web site (http://www.nature.com) or as paper copy from the London editorial office of *Nature*.

Acknowledgements. S.F.B.T., P.A.S. and computer time were funded by the Department of the Environment, Transport and the Regions. W.J.I. and J.F.B.M. were supported by the UK Public Meteorological Service Research and Development programme. M.R.A. was supported by a research fellowship from the UK Natural Environment Research Council. Supplementary support was provided by the European Commission.

Correspondence and requests for materials should be addressed to S.B.F.T. (3-mail: sfbtett@meto.gov.uk).

Changing spatial structure of the thermohaline circulation in response to atmospheric CO_2 forcing in a climate model

Richard A. Wood, Ann B. Keen, John F. B. Mitchell & Jonathan M. Gregory

Hadley Centre for Climate Prediction and Research, Meteorological Office, London Road, Bracknell RG12 2SY, UK

The heat transported northwards by the North Atlantic thermohaline circulation warms the climate of western Europe[1–3]. Previous model studies[4–6] have suggested that the circulation is sensitive to increases in atmospheric greenhouse-gas concentrations, but such models have been criticised for the use of unphysical 'flux adjustments'[7–9] (artificial corrections that keep the model from drifting to unrealistic states), and for their inability to simulate deep-water formation both north and south of the Greenland–Iceland–Scotland ridge, as seen in observations[10,11]. Here we present simulations of today's thermohaline circulation using a coupled ocean–atmosphere general circulation model without flux adjustments. These simulations compare well with the observed thermohaline circulation, including the formation of deep water on each side of the Greenland–Iceland–Scotland ridge. The model responds to forcing with increasing atmospheric greenhouse-gas concentrations by a collapse of the circulation and convection in the Labrador Sea, while the deep-water formation north of the ridge remains stable. These changes are similar in two simulations with different rates of increase of CO_2 concentrations. The effects of increasing atmospheric greenhouse-gas concentrations that we simulate are potentially observable, suggesting that it is possible to set up an oceanic monitoring system for the detection of anthropogenic influence on ocean circulation.

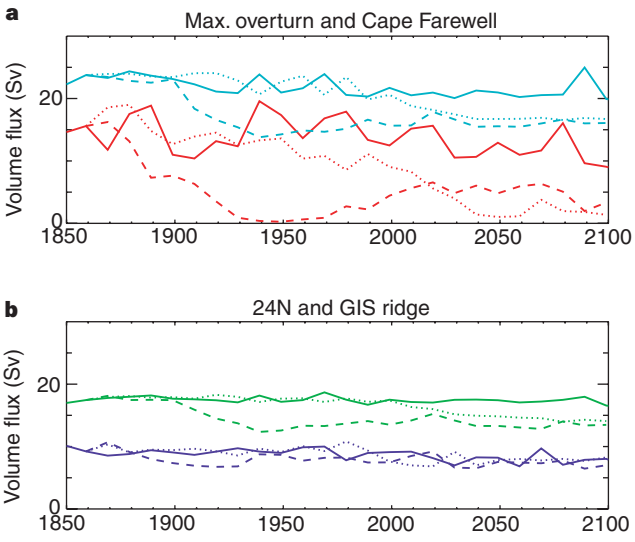

Figure 1 Time series of various components of the thermohaline circulation. **a**, Maximum meridional overturning at all latitudes in the North Atlantic (light blue), and volume flux of water denser than $\sigma_\theta = 27.5$ across Cape Farewell (red); **b**, maximum meridional overturning at 24° N (green), and volume flux of water denser than $\sigma_\theta = 27.5$ across the GIS ridge (dark blue). These time series are shown for the control (solid lines), 2PC (dashed lines) and GHG (dotted lines) runs. The GIS ridge, Cape Farewell and 24° N sections are shown in Fig. 4a. The initial 100 years of spinup of the control run are not shown.

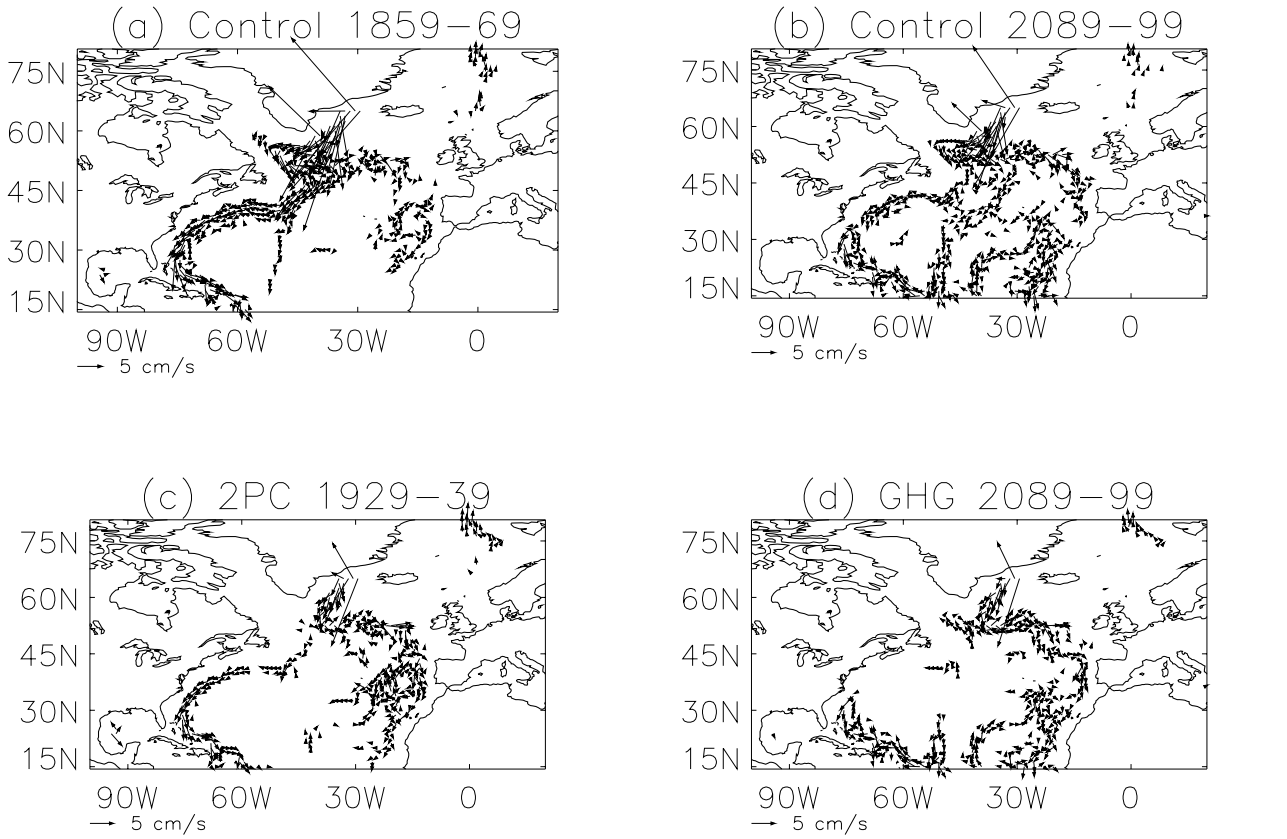

Figure 2 Decadal mean velocity in the North Atlantic at 2,731 m depth. **a**, Control run 1859–69; **b**, control run 2089–99; **c**, 2PC 1929–39; **d**, GHG 2089–99. For clarity, only velocities greater than 0.7 cm s^{-1} are shown. A scale vector is shown at the bottom left of each panel.

The model that we use, HadCM3, is a coupled atmosphere–ocean–sea ice general circulation model developed from an earlier version used extensively for climate studies[12]. Specific changes include increased ocean horizontal resolution (from 3.75 × 2.5 degrees longitude × latitude to 1.25 × 1.25 degrees), and inclusion of a modified convection scheme in regions of dense overflows[13] and the Gent–McWilliams[14] adiabatic diffusion scheme. The increased resolution allows us to represent the channels in the Greenland–Iceland–Scotland (GIS) ridge through which the dense overflow water from the Greenland, Iceland and Norwegian (GIN) seas passes into the North Atlantic. These overflows are known to influence the structure of the whole North Atlantic circulation[15]. Atmospheric model improvements include a new radiation scheme, and revisions to the cloud, convection, boundary layer and land surface schemes. See ref. 16 for model details.

To investigate the sensitivity of the thermohaline circulation to changes in atmospheric concentrations of greenhouse gases we perform three integrations of the model. The control simulation begins from the present-day ocean state[17] and is run for 340 years, with greenhouse-gas concentrations fixed at pre-industrial values. The nominal start date of the run is 1759, and results are presented below for years 1859–2100 (that is, following a 100-year spinup period). Runs 2PC and GHG begin from the control state at 1859 and are forced with different scenarios of increasing atmospheric CO_2. In 2PC, CO_2 is increased by 2% per year until 1929 (when it reaches four times the control value), and is held constant thereafter. This represents an unrealistically fast CO_2 increase, to highlight the sensitivity of the circulation. Run GHG follows historical concentrations of all anthropogenic greenhouse gases from 1859 to the present, followed by the IS92a 'business as usual' concentration scenario to 2100[18]. Calendar dates are only significant for run GHG.

We first describe the control simulation. The model's large-scale ocean heat transports agree with observational estimates and with those implied by the surface heat fluxes produced by the atmospheric component alone[16], allowing a stable, realistic surface climate without use of flux adjustments[16,19,20]. The maximum overturning in the North Atlantic has a mean value of 21.6 Sv over the period 1859–2100, with little secular trend (Fig. 1a). Although this quantity is frequently used by modellers as a measure of the strength of the thermohaline circulation, it cannot in practice be estimated from observations. We therefore diagnose the formation and transport of North Atlantic Deep Water at three important locations where there are relatively robust observations: the GIS ridge (GIN seas overflow), south of Cape Farewell (the southern tip of Greenland), and the transatlantic section at 24° N. For the GIS ridge the mean flow is 8.5 Sv, compared with the observational estimate[11] of 5.6 Sv (Fig. 1b). The model North Atlantic is somewhat too salty, and hence the overflow density of $\sigma_\theta = 28.3$ is higher than the observed value[11] of 28.0. At Cape Farewell, the transport shows interdecadal variability with a magnitude and timescale which is consistent with a recent reconstruction based on historical hydrographic data[21] (Fig. 1a). The model's mean transport is 13.0 Sv, consistent with the only direct current-meter measurements at this section[22]. At 24° N the model flow is 17.4 Sv, compared with the observational estimate[2] of 19.3 Sv (Fig. 1b). Thus the model gives a reasonable quantitative simulation of the flow of North Atlantic Deep Water, and in particular the partition of the flow between sources to the north and south of the GIS ridge. None of the section transports shows marked secular drift over the period 1859–2100, although there is some drift in the vertical structure of the flow at 24° N due to gradual intrusion of Antarctic Bottom Water[16].

Next we discuss results from run 2PC. The maximum overturning (occurring at about 30° N) falls from around 23 Sv to 14 Sv as CO_2 is increased, then recovers slightly after 1929 (Fig. 1a). This is

qualitatively similar to some earlier studies[5,6], but the circulation does not collapse completely as it did in an earlier 4 × CO_2 simulation using the GFDL model[4]. This difference may be linked to a weaker increase of freshwater input to the North Atlantic in HadCM3 than in the GFDL model. The 'hydrological sensitivity'[23] k of HadCM3 is 0.023 Sv K^{-1}, compared with 0.03 Sv K^{-1} for the GFDL model[23]. For HadCM3, k includes a contribution of 0.003 Sv K^{-1} from increased melting of the Greenland ice sheet. This agrees well with estimates based on more sophisticated ice-sheet models[24]. Unlike previous studies, there is no possibility here that the circulation is artificially stabilized or destabilized through a large proportion of the surface heat and freshwater flux being contained in (fixed) flux adjustment terms, which cannot vary as the forcing and circulation change[9]. For this reason, we believe that we can have more confidence in the mechanisms of thermohaline circulation change produced by our model.

The changes in maximum overturning are reflected in the overturning at 24° N which drops by 20–25% by the time of CO_2 quadrupling (Fig. 1b). The volume flux across the GIS ridge is relatively stable throughout the run (Fig. 1b), although the outflow water becomes warmer and lighter as the climate warms. The main changes in the deep circulation take place south of the GIS ridge. The cyclonic circulation in the Labrador Sea (Fig. 2a, b) collapses completely by the time of CO_2 quadrupling (Fig. 2c). This is reflected in a collapse of the flow across the Cape Farewell section (Fig. 1a). The deep Labrador Sea circulation is driven by the density contrast between the dense overflow water entering the Labrador basin at Cape Farewell and the lighter water in the interior Labrador basin. As a result of surface warming in the GIN seas, the GIS overflow water becomes lighter through the run (mean density $\sigma_\theta = 28.3$ at the start of the run to $\sigma_\theta = 28.1$ in 1929), and this is reflected downstream in the density of the deep boundary current northeast of Cape Farewell (Fig. 3a, c, segment CD). The interior Labrador water (Fig. 3a, c, segment BC) is less strongly ventilated, so its density changes less; by 1929 the deep boundary current water is no denser than the interior water, so there is no longer a pressure gradient to drive the deep water around the Labrador Sea.

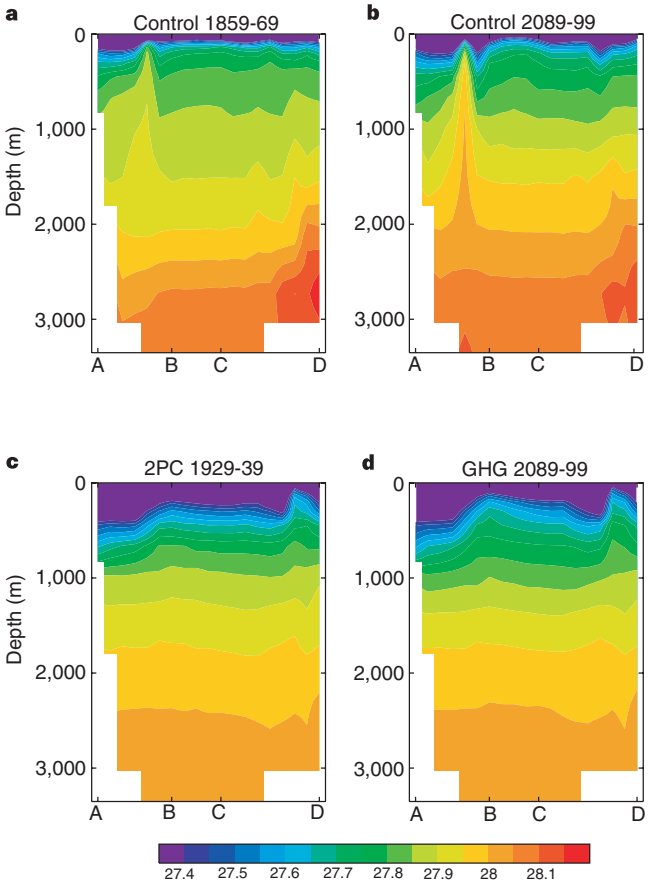

Figure 3 Potential density σ_θ (kg m^{-3}) on section ABCD. The section is shown in Fig. 4a. The segment DC follows approximately the core of the dense overflow water from Denmark Strait. The doming between A and B is evidence of convection in the Labrador Sea. There is some drift in the control run on this section (compare **a** and **b**) but the stronger doming in **b** is partly due to interdecadal variability in the control run.

Further northwest in the Labrador Sea is a site of convection, shown by the doming of density surfaces in Fig. 3a, segment AB. Labrador Sea water formed here contributes to the southward flowing North Atlantic Deep Water at 24° N[3]. In the control run, the convection varies on interdecadal timescales, as observed[25] (compare Figs 3a and b), but by 1929 in 2PC (Fig. 3c) the convection has ceased as a result of surface freshening and warming.

To summarize, the amount of overflow of deep water across the GIS ridge appears remarkably insensitive to the CO_2 increase, but because the overflow water becomes lighter than the interior deep Labrador Sea its circulation around the Labrador Sea collapses. Convection in the Labrador Sea also stops. These changes are reflected further downstream at 24° N, where the NADW flow is reduced by ~20%.

In GHG, the imposed radiative forcing at 2089 is approximately equivalent to CO_2 quadrupling, and the flow changes are qualitatively and quantitatively similar to those in 2PC in 1929 (Figs 1, 2d, 3d). Thus the circulation changes appear robust, and the final state appears to be not strongly dependent on the time profile of greenhouse-gas increase in this case, at least up to 2100[26]. In GHG, the Labrador Sea convection collapse occurs around 1999–2029 (we note that GHG does not include all forcings, for example, the mitigating effect of sulphate aerosols which would delay the response).

By the time of CO_2 quadrupling, the sea surface temperature has increased by several degrees over most of the North Atlantic (Fig. 4), and the climate of western Europe has warmed substantially. However the ocean warming is a minimum, with even some regions of cooling (in the northeast Atlantic and Greenland Sea), suggesting that the changes in thermohaline circulation are important in modifying the surface response to the greenhouse-gas increase.

A number of factors should be borne in mind concerning our results. First, there is a slight drift in the density field through the control run (Fig. 3a, b); but this drift is smaller than the density changes in the overflow water (Fig. 3c, d). Second, the model's GIS overflows take place through grid-scale channels. Most of the model overflow passes through the Denmark Strait between Greenland and Iceland, whereas a significant proportion of this flow is observed to the east of Iceland[11]. In reality, the channels are narrower than the model grid scale, but previous model studies suggest that the sill depths, and not their widths, may control the flow[27]. It is clearly important to improve understanding of the physics and modelling of overflow processes, given their fundamental influence on the thermohaline circulation[15,28]. Third, because the deep-water formation is localized in the model (as in reality), the changes in thermohaline circulation may depend on relatively small-scale features of the atmospheric response, which vary between general circulation models[24]. Last, the sensitivity of the hydrological cycle to climate change is an important factor in the response of the thermohaline circulation, and remains subject to both observational and modelling uncertainty[23].

Despite the above uncertainties, we believe that the HadCM3 model has reached a level of realism where it can give valuable information on possible future changes in thermohaline circulation. This not only leads to more confident predictions of climate change, but can also inform the design of monitoring systems for oceanic climate change. Our results suggest a clear spatial pattern

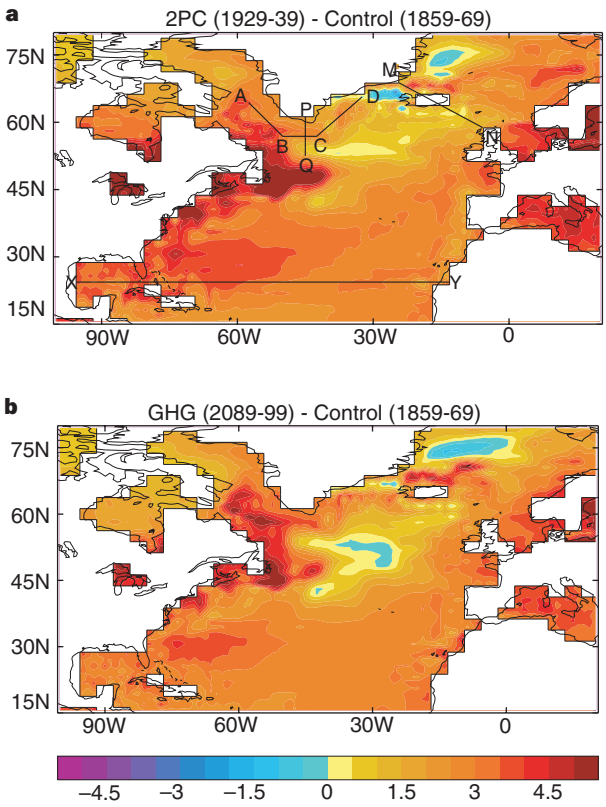

Figure 4 Changes in decadal mean sea surface temperature (°C). **a**, Difference between 2PC run 1929–39 and control 1859–69; **b**, difference between GHG run 2089–99 and control 1859–69. In **a** are also shown the approximate paths of the sections used in Fig. 1 (the GIS ridge (MN), Cape Farewell (PQ), 24° N (XY)) and Fig. 3 (ABCD).

for the response of the ocean thermohaline circulation to CO_2 forcing. If this pattern is robust, a monitoring system based on repeated hydrographic sections in the Labrador Sea and at 24° N, and current-meter measurements of the GIS overflows and the Cape Farewell boundary current, could provide a means of detection of changes in thermohaline circulation resulting from increased greenhouse-gas forcing. Much of this would build on the existing historical database[11,21,22,29,30]. The extent to which such a signal could be detected at present depends on the natural variability in these elements of the circulation, which has not yet been fully quantified from observations. □

Received 6 November 1998; accepted 26 March 1999.

1. Manabe, S. & Stouffer, R. J. Two stable equilibra of a coupled ocean-atmosphere model. *J. Clim.* **1,** 841–866 (1988).
2. Hall, M. M. & Bryden, H. L. Direct estimates of ocean heat transport. *Deep Sea Res.* **29,** 339–359 (1982).
3. Roemmich, D. & Wunsch, C. Two transatlantic sections: meridional circulation and heat flux in the subtropical North Atlantic Ocean. *Deep Sea Res.* **32,** 619–664 (1985).
4. Manabe, S. & Stouffer, R. J. Century-scale effects of increased atmospheric CO_2 on the ocean–atmosphere system. *Nature* **364,** 215–218 (1993).
5. Murphy, J. M. & Mitchell, J. F. B. Transient response of the Hadley Centre coupled model to increasing carbon dioxide. Part II. Temporal and spatial evolution of patterns. *J. Clim.* **8,** 57–80 (1995).
6. Cubasch, U. *et al.* Time-dependent greenhouse warming computations with a coupled ocean-atmosphere model. *Clim. Dyn.* **8,** 55–69 (1993).
7. Rahmstorf, S. Risk of sea-change in the Atlantic. *Nature* **388,** 825–826 (1997).
8. Houghton, J. T. *et al.* (eds) *Climate Change 1995: the Science of Climate Change* (Cambridge Univ. Press, 1996).
9. Marotzke, J. & Stone, P. H. Atmospheric transports, the thermohaline circulation, and flux adjustments in a simple coupled model. *J. Phys. Oceanogr.* **25,** 1350–1364 (1995).
10. Rahmstorf, S. Bifurcations of the Atlantic thermohaline circulation in response to changes in the hydrological cycle. *Nature* **378,** 145–149 (1995).
11. Dickson, R. R. & Brown, J. The production of North Atlantic Deep Water: sources, rates and pathways. *J. Geophys. Res.* **99,** 12319–12341 (1994).
12. Johns, T. C. *et al.* The second Hadley Centre coupled ocean-atmosphere GCM: model description, spinup and validation. *Clim. Dyn.* **13,** 103–134 (1997).
13. Roether, W., Roussenov, V. M. & Well, R. in *Ocean Processes in Climate Dynamics: Global and Mediterranean Examples* (eds Malanotte-Rizzoli, P. & Robinson, A. R.) 371–394 (Kluwer, Dordrecht, 1994).
14. Gent, P. & McWilliams, J. C. Isopycnal mixing in ocean circulation models. *J. Phys. Oceanogr.* **20,** 150–155 (1990).
15. Roberts, M. J. & Wood, R. A. Topgraphic sensitivity studies with a Bryan-Cox type ocean model. *J. Phys. Oceanogr.* **27,** 823–836 (1997).
16. Gordon, C. *et al.* The simulation of SST, sea ice extents and ocean heat transports in a version of the Hadley Centre coupled model without flux adjustments. *Clim. Dyn.* (in the press).
17. Levitus, S. & Boyer, T. P. *World Ocean Atlas 1994* (NOAA/NESDIS E/OC21, US Dept of Commerce, Washington DC, 1994).
18. Houghton, J. T. *et al.* (eds) *Climate Change 1992: the Supplementary Report to the IPCC Scientific Assessment* (eds Houghton, J. T., Meira Filho, L. G., Callander, B. A., Harris, N., Kattenberg, A. & Maskell, K.) (Cambridge Univ. Press, 1996).
19. Weaver, A. J. & Hughes, T. M. C. On the incompatibility of ocean and atmosphere models and the need for flux adjustments. *Clim. Dyn.* **12,** 141–170 (1996).
20. Bryan, F. O. Climate drift in a multi-century integration of the NCAR Climate System Model. *J. Clim.* **11,** 1455–1471 (1998).
21. Bacon, S. Decadal variability in the outflow from the Nordic seas to the deep Atlantic Ocean. *Nature* **394,** 871–871 (1998).
22. Clarke, R. A. Transport through the Cape Farewell–Flemish Cap section. *Rapp. P.-v. Réun. Cons. Int. Explor. Mer.* **185,** 120–130 (1984).
23. Rahmstorf, S. & Ganopolski, A. Long-term global warming scenarios computed with an efficient coupled climate model. *Clim. Change* (in the press).
24. *IPCC Workshop Report on Rapid Non-linear Climate Change* (Intergovernmental Panel on Climate Change, Bracknell, 1998).
25. Dickson, R., Lazier, J., Meincke, J., Rhines, P. & Swift, J. Long-term coordinated changes in the convective activity of the North Atlantic. *Prog. Oceanogr.* **38,** 241–295 (1996).
26. Stocker, T. F. & Schmittner, A. Influence of CO_2 emission rates on the stability of the thermohaline circulation. *Nature* **388,** 862–865 (1997).
27. Wadley, M. R. & Bigg, G. R. Abyssal channel flow in ocean general circulation models with application to the Vema Channel. *J. Phys. Oceanogr.* **26,** 38–48 (1996).
28. Doescher, R. & Redler, R. The relative importance of northern overflow and subpolar deep convection for the North Atlantic thermohaline circulation. *J. Phys. Oceanogr.* **27,** 1894–1902 (1997).
29. Parilla, G., Lavin, A., Bryden, H. L., Garcia, M. & Millard, R. Rising temperatures in the subtropical North Atlantic Ocean over the past 35 years. *Nature* **369,** 48–51 (1994).
30. Lazier, J. R. N. in *Natural Climate Variability on Decade-to-century Timescales* (eds Martinson, D. G. *et al.*) 295–302 (Nat. Academy Press, Washington DC, 1995).

Acknowledgements. We thank H. Cattle, G. Jenkins, J. Murphy, S. Rahmstorf, R. Stouffer, R. Thorpe and A. Weaver for comments. This work was supported by the UK Department of the Environment, Transport and the Regions.

Correspondence and requests for materials should be addressed to R.A.W. (e-mail: rwood@meto.gov.uk)

Feature-based attention influences motion processing gain in macaque visual cortex

Stefan Treue & Julio C. Martínez Trujillo

Cognitive Neuroscience Laboratory, Department of Neurology, University of Tübingen, Auf der Morgenstelle 15, 72076 Tübingen, Germany

Changes in neural responses based on spatial attention have been demonstrated in many areas of visual cortex[1–4], indicating that the neural correlate of attention is an enhanced response to stimuli at an attended location and reduced responses to stimuli elsewhere. Here we demonstrate non-spatial, feature-based attentional modulation of visual motion processing, and show that attention increases the gain of direction-selective neurons in visual cortical area MT without narrowing the direction-tuning curves. These findings place important constraints on the neural mechanisms of attention and we propose to unify the effects of spatial location, direction of motion and other features of the attended stimuli in a 'feature similarity gain model' of attention.

We studied the influence of attention on the sensory selectivity of neurons in visual cortex, namely direction-selective neurons in the middle temporal visual area (MT), which is important in the perception of visual motion and for motor planning[5,6]. MT neurons have been linked directly to psychophysical performance in motion tasks[7] and they characteristically show direction tuning curves (bell-shaped response profiles as a function of stimulus direction; Fig. 1b), which account well for psychophysical thresholds of motion perception[8].

We recorded from neurons in area MT of two macaque monkeys while using displays of coherently moving random dot patterns (RDP) to determine what effect attention might have on these direction tuning curves. Attention might enhance the sensory gain of the neuron, that is, increase the response to all attended stimuli by the same proportion ('multiplicative modulation'), leaving the